



Numerical investigation of heat transfer and erosion characteristics for H-type finned oval tube with longitudinal vortex generators and dimples



X.B. Zhao, G.H. Tang*, X.W. Ma, Y. Jin, W.Q. Tao

MOE Key Laboratory of Thermo-Fluid Science and Engineering, School of Energy and Power Engineering, Xi'an Jiaotong University, Xi'an 710049, PR China

HIGHLIGHTS

- We consider heat transfer, flow character and erosion character of heat exchanger.
- We investigate hybrid effect on comprehensive performance for compound dimple and LVG.
- Hemisphere protrusions on oval tube inspired from anti-wear bionics can reduce erosion greatly.

ARTICLE INFO

Article history:

Received 29 November 2013
Received in revised form 1 April 2014
Accepted 10 April 2014

Keywords:

Heat transfer
Erosion
Longitudinal vortex generators
Dimple

ABSTRACT

To improve heat transfer performance and reduce erosion of economizers in coal-fired power plants, firstly the heat transfer and erosion characteristics is numerically studied for the single H-type finned oval tube with enhanced heat transfer structures including bleeding dimples, longitudinal vortex generators (LVGs), and compound dimple-LVG. The simulation results show that the oval tube with compound LVG-dimple achieves the highest overall heat transfer performance while the oval tube with LVG works most efficiently in the anti-wear performance. Then based on the H-type finned oval tube, the LVG structure on the first row of tubes together with hemisphere protrusions design, while the compound LVG-dimple on the rest tubes are also simulated. The optimized H-type finned oval tube bank heat exchanger is demonstrated of high performance on both heat transfer and anti-wear.

© 2014 Elsevier Ltd. All rights reserved.

1. Introduction

For the heat recovery from flue gas, the heat exchanger is usually designed in which the energy is transferred from the shell-side flue gas to the tube-side water. The heat transfer enhancement inside tube has received much attention and lots of new techniques have been investigated and applied in engineering [1–3]. However, the energy transfer outside tube of economizers in coal-fired boilers needs more attention and usually faces two significant problems: low heat transfer efficiency of the gas, and serious tube erosion caused by ash and particles from coal combustion. Recently, longitudinal vortex generators (LVGs) and dimples have been proved to have a high performance in shell-side gas heat transfer enhancement. Zhang et al. [4] experimentally compared the fin tube bank with mounted LVGs and the fin tube bank with punched LVGs by the naphthalene sublimation way. The results indicated that in the case of very small area ratio of LVG surface to fin surface, the finned tubes with punched LVGs and with

mounted LVGs have almost the same heat transfer and pressure drop. Joardar and Jacobi [5] experimentally studied the heat transfer and pressure drop both in plain finned tube with mounted 3 LVGs in-line array and with mounted one LVG in leading edge. Promvong and Thianpong [6] experimentally investigated the heat transfer and friction loss for turbulent airflow through a constant heat flux channel combined with ribs and winglet-type LVGs. Tian et al. [7] conducted numerically a comparative study on the air-side performance of wavy finned tube heat exchanger with punched delta winglets both in staggered and in-line arrangements. Their results show that different arrangements of tube bank perform different enhanced heat transfers. Li et al. [8] studied the heat transfer and laminar flow characteristics of a slit finned tube heat exchanger with LVGs numerically. They also optimized the slit fin structure by using the field synergy principle. He et al. [9] numerically investigated heat transfer and pressure drop for the finned tube heat exchanger with two different delta winglet vortex generators arrays and explored the basic mechanism between the local flow characteristics and the heat transfer enhancement, including the effects of attack angles of delta winglet pairs, and layout locations of delta winglet pairs. Bilir et al. [10] designed

* Corresponding author. Tel.: +86 29 82665319; fax: +86 29 82665445.
E-mail address: ghtang@mail.xjtu.edu.cn (G.H. Tang).

Nomenclature

A_t	total surface area (m^2)	Re	Reynolds number
A_m	minimum flow cross-section area (m^2)	Re_m	relative particle Reynolds number
a	length of the oval tube major radius (m)	r_1	radius of the dimple (m)
b	length of the oval tube minor radius (m)	r_2	radius of the bleeding hole (m)
a_m	width of the rectangle punching (m)	r_3	radius of the hemisphere protrusion (m)
b_m	length of the rectangle punching (m)	S_1	spanwise tube pitch (m)
C_p	specific heat capacity ($J\ kg^{-1}\ K^{-1}$)	S_2	longitudinal tube pitch (m)
d_p	particle diameter (m)	T	temperature (K)
Eu	Euler number	u	velocity ($m\ s^{-1}$)
E_{tube}	erosion loss of tube (mg/g)	W	length of the dimple to center (m)
F_m	spanwise winglet pitch (m)	w	fin width (m)
F_i, F_n	spanwise dimple pitch (m)		
F_t	fin pitch (m)	<i>Greek</i>	
F_p	fin thickness (m)	ρ	density ($kg\ m^{-3}$)
f	friction factor	λ	thermal conductivity ($W\ m^{-1}\ K^{-1}$)
H	fin height (m)	ε	turbulent energy dissipation rate ($m^2\ s^{-3}$)
H_m	height of the rectangle winglet (m)	μ	dynamic viscosity ($kg\ m^{-1}\ s^{-1}$)
h	heat transfer coefficient ($W\ m^{-2}\ K^{-1}$)	β	angle between particle path and tube surface ($^\circ$)
k	turbulent kinetic energy ($m^2\ s^{-2}$)		
m	slit width (m)	<i>Subscripts</i>	
Nu	Nusselt number	in	inlet
P	pressure (Pa)	out	outlet
PEC	evaluation parameter of a heat transfer unit	m	maximum
Pr	Prandtl number	w	wall
Q	heat transfer capacity (W)		

finned tube heat exchangers with three types of vortex generators, and analyzed the individual influence of each vortex generator, as well as the hybrid influence on the heat transfer. Wu et al. [11] studied the airside convective heat transfer performance of two-row finned tubes with punched longitudinal vortex generators experimentally. It is found that one can achieve heat transfer enhancement with a reduction of pressure loss by the strategies of fin-tube surface with longitudinal vortex generator design and appropriate placement on the fin-tube surface. Yakut et al. [12] conducted experimental study on heat transfer and flow characteristics of the tapes with double-side delta-winglets under different geometric and flow parameters. They obtained the optimum parameters using the Taguchi experimental-design method. Pesteei et al. [13] made an experiment to study the effect of winglet location on heat transfer of the fin-tube and obtained the best winglet location with respect to the case in their paper. Chen et al. [14–16] presented a three dimensional numerical simulation to study the heat transfer of a finned oval tube with both staggered and aligned punched longitudinal vortex generators. The effects of attack angle and the aspect ratio of a winglet were also examined. Yang et al. [17] experimentally investigated the pressure drop and heat transfer characteristics of different dimple vortex generator arrangements in plain fin. Vicente et al. [18] experimentally studied the heat transfer and friction characteristics of the helically dimpled tubes. Bi et al. [19] numerically studied the convective heat transfer inside mini-channels with dimples, cylindrical grooves and low fins. They found that the dimple surface shows the highest performance of heat transfer enhancement. Lee et al. [20] numerically studied the heat transfer and laminar or turbulent flow characteristics in a plate heat exchanger with dimple and protrusion and a correlation for the critical Reynolds number from laminar or turbulent flow was obtained.

To reduce the tube wear loss in economizers, Grant and Tabkoff [21] used a Monte Carlo simulation to predict the erosion of particles collided with rotating machinery. Hutchings and Winter [22] observed the coarse metal surface after being impacted by

spherical solid particles with an electron microscope, and it is concluded that material removal mechanism occurs on the metal surface along the particle movement direction. Winter and Hutchings [23] investigated the effect of the particle impact angle on the wear by experiments. Nagarajan et al. [24] determined the effects of ash particle physical properties and transport dynamics on the erosive wear of three different grades of low alloy steel experimentally. Lee et al. [25] used Eulerian approach, which is more simple and economic than the Lagrangian approach, to predict the erosion of single tube. A three-dimensional modeling was performed by Rahimi et al. [26] by using an in-house computational fluid dynamics (CFD) code to explore the reason for tube damage in heat exchangers in power plants. Simulation results show that the fly ash particle size, concentration, speed impact angle and metal surface roughness have effects on erosion mechanism. Schade et al. [27] experimentally investigated the effects of impact velocity and angle on the particle-wall erosion. Based on the experimental data, a three-dimensional numerical simulation of wear of the pipework in a coal-fired power plant was performed. Wang and Yang [28] studied the effects of impact angle, impact velocity and particle penetration on the target erosion loss on both ductile and brittle materials with the finite element model. Sundararajan and Roy [29] reviewed the prominent feature of solid particle erosion behavior related to room temperature and elevated temperature erosion of metallic materials. Fan et al. [30–33] made a series of numerical calculation to predict the interaction between particles and tubes and the erosion. In these researches, some anti-wear structures were presented. Dodds and his co-workers [34,35] investigated the distribution of gas and particle mass flow through the mill-duct system of a real-life operating power station to improve the boiler efficiency of the power station both numerically and experimentally. The wear of the mill-duct system caused by different raw coal (containing different percentage of sand loading) under normal operating conditions was numerically predicted. Their results show that the particle ropes twist around perimeter of duct with a lot of bends being encountered.

However, for the heat transfer enhancement techniques all above, usually the sole LVG or the dimple is adopted. In the present research, we combine the two enhanced heat transfer techniques to study the hybrid mechanism. In particular, for heat exchangers in the coal-fired power plants, it is necessary to consider not only the heat transfer and flow resistance performance, but also the anti-wear performance. In this paper, firstly, we study the heat transfer and erosion characteristics of the single H-type finned oval tube, the H-type finned oval tube with bleeding dimples, with -30° rectangular LVGs, and with compound dimples and LVGs. Then, numerical study is performed for the heat transfer and erosion characteristics of an optimized H-type five-row finned oval tube bank. Features of the optimized heat exchanger include the first row of the oval tube with both LVGs and bionic protrusions fabricated on the windward, while the rest rows with compound dimple-LVG, which could improve the heat transfer as much as possible, as well as reduce the wear loss. The purpose of this paper is to study the mechanism of heat transfer enhancement and erosion reduction of H-type finned oval tube bank with different vortex generators so that we can achieve a high efficient heat exchanger on both heat transfer enhancement and anti-erosion.

2. Model description and numerical method

2.1. Physical model

A schematic diagram of a novel H-type five-row finned oval tube bank with compound dimples and LVGs is displayed in Fig. 1. The origin point ($x = y = z = 0$) locates at the geometry center of the physical model. The design of the tube row conforms to the nonuniformity design rule, that is, the first row adopts LVGs for anti-erosion purpose while the rest rows use the compound LVG-dimple for heat transfer enhancement. At the same time, to reduce the erosion loss of the first row of tube more effectively, inspired by the anti-erosion bionics, we design hemisphere protrusions in the windward side of the first row of tube as shown in Fig. 2(b). Fig. 2(c) presents the surface morphology of *Laudakia stoliczka*, a desert lizard of excellent anti-erosion function living in the sand environment. A pair of rectangle winglets is punched out from the fin symmetrically behind each oval tube and the bleeding dimples are penetrated out in the windward side. The geometry parameters of the H-type finned oval tube with dimple and -30° rectangular

LVGs are listed in Fig. 2 and Table 1. Note that the dimple in the present study is different from a usual one by making a bleed hole inside the dimple cavity to let the fluid flow through it.

2.2. Governing equations and boundary conditions

It is assumed that the gas–solid flow in the economizer is a three-dimensional, viscous and steady incompressible turbulent flow. The tube surface is assumed to be at a constant temperature $T_w = 350$ K and the wall thickness is ignored due to the relatively large heat transfer coefficient between the cooling water and inner wall of the tubes and the high thermal conductivity of the tube wall. Moreover, the temperature distribution in the fin surface and in the gas fluid is determined by coupled computation. The solid fin and tube are assumed to have constant thermal conductivity.

2.2.1. Gas-phase governing equations

The gas-phase governing equations including mass, momentum and energy conservation equations are as follows.

Continuity equation:

$$\frac{\partial}{\partial x_i}(\rho u_i) = 0 \tag{1}$$

Momentum equation:

$$\frac{\partial}{\partial x_i}(\rho u_i u_j) = \frac{\partial}{\partial x_i} \left(\mu \frac{\partial u_j}{\partial x_i} \right) - \frac{\partial p}{\partial x_j} \tag{2}$$

Energy equation:

$$\frac{\partial}{\partial x_i}(\rho u_i T) = \frac{\partial}{\partial x_i} \left(\frac{\lambda}{C_p} \frac{\partial T}{\partial x_i} \right) \tag{3}$$

For the turbulence model, Speziale and Thangam [36] investigated the gas flow over a backward facing step, and the produced complex shear flow with separation from the RNG $k-\epsilon$ model is very close to the experimental measurement. Tian et al. [7] predicted the complicated separated flow over wave finned tube with LVGs by comparing the laminar model, standard $k-\epsilon$ model and RNG $k-\epsilon$ model. The results of the RNG $k-\epsilon$ model are in best agreement with experimental data. Therefore, the RNG $k-\epsilon$ turbulence

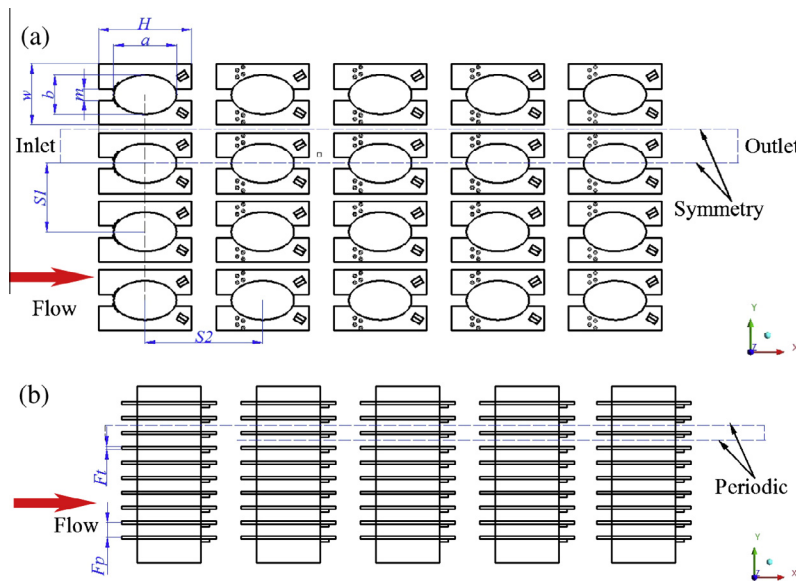


Fig. 1. Schematic of H-type finned oval tube heat exchanger. (a) Top view. (b) Side view.

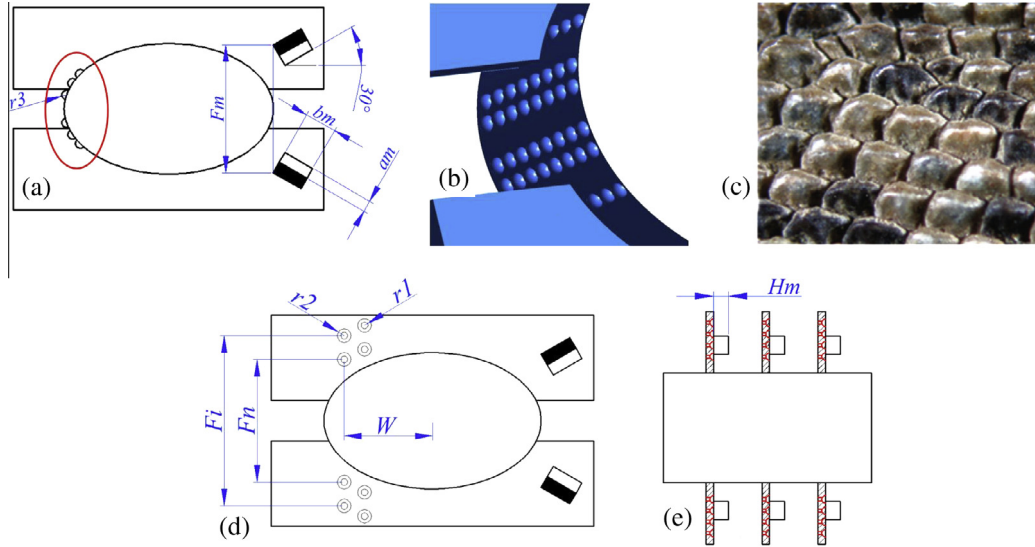


Fig. 2. Schematic of the heat exchanger unit. (a) The first row of finned tube with LVGs. (b) Zoom of the hemisphere protrusions. (c) Surface morphology of *Laudakia stoliczkana*. (d) The rest rows of tubes with dimple-LVG. (e) The side view of the bleeding dimples on the rest rows of tubes with dimple-LVG.

Table 1
Geometry parameters of the basic H-type finned oval tube with dimples and -30° LVGs.

a/mm	b/mm	S_1/mm	S_2/mm	H_m/mm
64	40	140	100	5
F_d/mm	F_m/mm	F_{pl}/mm	a_m/mm	b_m/mm
3	40	15	5	10
r_1/mm	r_2/mm	r_3/mm	H/mm	w/mm
1	0.4	1	95	72
F_n/mm	F_i/mm	m/mm	W/mm	
36	50	12	26	

model is chosen in the present paper, though it is reported that the RNG $k-\varepsilon$ model failed in predicting accurately the flow separations.

The RNG $k-\varepsilon$ turbulence model:

$$\rho \frac{Dk}{Dt} = \frac{\partial}{\partial x_i} \left[\alpha_k \mu_{\text{eff}} \frac{\partial k}{\partial x_i} \right] + \mu_t S^2 - \rho \varepsilon \quad (4)$$

$$\rho \frac{D\varepsilon}{Dt} = \frac{\partial}{\partial x_i} \left[\alpha_\varepsilon \mu_{\text{eff}} \frac{\partial \varepsilon}{\partial x_i} \right] + C_{1\varepsilon} \frac{\varepsilon}{k} \mu_t S^2 - C_{2\varepsilon} \rho \frac{\varepsilon^2}{k} - R \quad (5)$$

where R is the rate of strain term given by

$$R = \frac{C_\mu \rho \phi^3 (1 - \phi/\phi_0) \varepsilon^2}{1 + \beta \phi^3} \frac{\varepsilon^2}{k} \quad (6)$$

where $\phi = sk/\varepsilon$, $\phi_0 = 4.38$, $\beta = 0.012$, $C_{1\varepsilon} = 1.42$ and $C_{2\varepsilon} = 1.68$. $S^2 = 2S_{ij}S_{ij}$ is the modulus of the rate of strain tensor expressed as $S_{ij} = \frac{1}{2}(\partial u_i/\partial x_j + \partial u_j/\partial x_i)$.

2.2.2. Lagrangian formulation for particle motion

The particles are assumed to be spherical massless points and we track each individual particle in the Lagrangian framework. In our assumption, the forces acting on the particles such as the gravity, thermophoretic force and Brownian force are ignored, but the Saffman lift [37] caused by the transverse velocity gradient is considered.

The force balance of the particles:

$$\frac{du_p}{dt} = F_D(u - u_p) + \frac{g_x(\rho_p - \rho)}{\rho_p} + F_x \quad (7)$$

where $F_D(u - u_p)$ is the particle drag force per unit mass

$$F_D = \frac{18\mu C_D Re}{\rho_p d_p^2} \quad (8)$$

$$Re_m = \frac{\rho d_p |u_p - u|}{\mu} \quad (9)$$

where u is fluid phase velocity, u_p is particle velocity, μ is dynamic viscosity of the fluid, ρ and ρ_p are density of the fluid and particle, respectively, d_p is particle diameter, C_D is the drag coefficient and Re_m is relative particle Reynolds number.

2.2.3. Particle wall collision model and wall wear model

When fly ash particles collide with the surface of the tube and fin, the ash particles will change the trajectory as schematic in Fig. 3. To follow the particle trail, the collision model proposed by Tabakoff et al. [38] for coal ash particle impacting on stainless steel surface is employed. Normal and tangential coefficients of

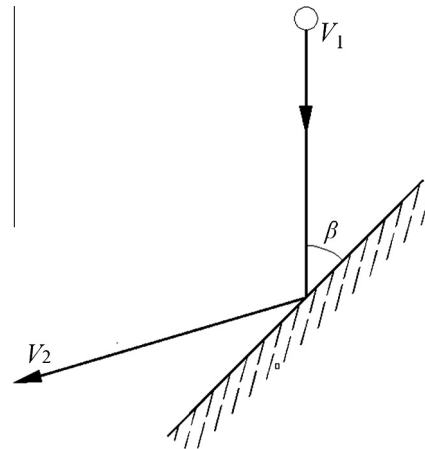


Fig. 3. Schematic of the particle collision with solid surface.

restitution can be assumed as constants during the collision of the particles with the tube and fin surface and presented as

$$\frac{V_{n2}}{V_{n1}} = 1.0 - 0.4159\beta - 0.4994\beta^2 + 0.292\beta^3 \quad (10)$$

$$\frac{V_{t2}}{V_{t1}} = 1.0 - 2.12\beta + 3.0775\beta^2 - 1.1\beta^3 \quad (11)$$

where V_n and V_t represent the particle velocity components normal and tangential to the tube surface, respectively. Subscripts 1 and 2 refer to the condition before and after collision, respectively. β is the angle between the incident velocity and the tangent to the surface as schematic in Fig. 3. In the erosion model by Tabakoff et al. [38], the mass wear rate E is defined as the ratio of the amount of mass loss of the target metal material (milligram) to the collision particle mass (gram).

$$E = K_1 \left\{ 1 + C_k \left[K_2 \sin \left(\frac{90}{\beta_0} \beta \right) \right] \right\}^2 V_i^2 \cos^2 \beta (1 - R_1^2) + K_3 (V_i \sin \beta)^4 \quad (12)$$

where V_i and β indicate the particle impact velocity and collision angle, respectively. $R_1 = 1 - 0.0016V \sin \beta$, and $\beta_0 = 25^\circ$ is the angle when the maximum erosion occurs according to the experimental results of Tabakoff et al. [38]. $C_k = 1$ for $\beta \leq 3\beta_0$, while $C_k = 0$ for $\beta > 3\beta_0$. K_1 , K_2 and K_3 are the empirical constants with $K_1 = 1.505101 \times 10^{-6}$, $K_2 = 0.296007$ and $K_3 = 5.0 \times 10^{-12}$. Here, the employed tube material and the particles are the AISI 304 stainless steel and the anthracite, respectively.

2.2.4. Boundary conditions

The computational domain is composed of six boundaries: inlet, outlet, two symmetrical boundary (right and left), and two periodic boundary surfaces (top and bottom) as schematic in Fig. 1. To maintain the uniform inlet velocity and avoid the exit velocity with a recirculation-free flow, the computational domain is extended along the upstream by 3.5 times of the oval tube major radius length at the inlet zone and along the downstream by ten times of the oval tube major radius length at the exit zone, respectively. At the inlet boundary, the flue gas enters the computational domain along the x direction at uniform velocity u_{in} , temperature T_{in} (450 K), and the velocity components along y and z directions are set to be zero. According to the Fluent User's Manual suggestion, the turbulent intensity $I = 0.16Re_{D_h}^{1/8}$. At the symmetry planes, the normal velocity component, the heat flux and the normal first derivatives of other variables are set to be zero. At the periodic planes, the velocity $u_{top} = u_{bottom}$, and the temperature $T_{top} = T_{bottom}$. At the outlet, the first order derivatives of the temperature, the velocity components along x , y and z directions in the streamwise direction are set to be zero.

As we know, the fluid flow plays a strong role in the motion of the particles, and the physical properties of particles have great influences on the erosion. So it is essential to set a clear description about particle characteristics. At the same time, the volume fraction of the particle phase, representing the volume occupied by the particle phase in unit volume, is an important parameter which determines the influence degree of the discrete phase on the continuous phase. Sommerfeld [39] proposed classifications for the discrete-continuous phase system according to the volume fraction of the particle phase. For the particle phase, the diameter distribution of particle group follows the Rosin-Rammler diameter distribution, which can be manifested that the maximum diameter, minimum diameter and mean diameter of particles are 0.03 mm, 0.0001 mm and 0.01 mm, respectively. Therefore, the particulate phase is considered to be a dilute phase according to Sommerfeld [39], and one-way coupling is applied in the dilute dispersed

two-phase flow, and the effect of the discrete phase on the continuous phase is ignored. Our preliminary work using two-way coupling also indicated that there is no difference in gas flow patterns from the one-way coupled results. Solnordal et al. [40] also compared the two coupling algorithms, and the results show that the one-way coupling between solid particles and air could predict the flow patterns accurately. When the particle-gas two phases are simulated by one-way coupling, the fluid phase is solved primarily and the particles are not added in the fluid field. When numerical computation of the fluid converges, the plane jet source of particles is added in the inlet surface, and the trail of particles is traced based on Lagrangian framework. In this paper, a three-dimensional and steady-state numerical simulation is conducted by using the commercial software FLUENT with a second-order discretization scheme for both convective and diffusive terms. The coupling calculation between the velocity and pressure is treated with SIMPLE algorithm. When the residual of each variable for gas phase is below 10^{-4} , the numerical computation is regarded as convergence. The motion of particles and erosion of tubes are measured by writing a UDF program.

2.3. Parameter definition

Some characteristic and non-dimensional parameters are defined as follows.

$$Re = \frac{\rho u_m D}{\mu}, \quad h = \frac{Q}{\Delta T A_t}, \quad Nu = \frac{hD}{\lambda}, \quad Eu = \frac{2\Delta p}{\rho u_m^2 Z},$$

$$\Delta T = \frac{(T_{out} - T_w) - (T_{in} - T_w)}{\ln((T_{out} - T_w)/(T_{in} - T_w))}, \quad f = \frac{2\Delta P A_m}{\rho u_m^2 A_t}, \quad \Delta P$$

$$= P_{in} - P_{out}, \quad PEC = \frac{Nu/Nu_0}{(f/f_0)^{1/3}} \quad (13)$$

In the above equations, u_m is average velocity in the minimum flow cross-section, Q is heat transfer capacity, ΔP is total pressure drop over the whole computational domain, Z is number of tube rows, A_m and A_t are minimum flow cross-section area, and total surface area, respectively, D is characteristic length, which is the length of the oval tube minor radius [41], and Nu_0 and f_0 are Nusselt number and friction factor of the compared baseline, respectively.

2.4. Grid generation and independence validation

Fig. 4 shows the schematic diagram of the generated mesh by using software GAMBIT 2.4.6. A multi-block hybrid method is adopted to generate the mesh. First, the whole computational domain is divided into four zones including the inlet, outlet, fluid and tube zones. Then different zones are employed with different grid generating shapes. For the inlet and outlet zone, we apply gradually thinner and gradually denser structured hexahedral mesh, respectively. The fluid zone is employed with finer structured hexahedral mesh to guarantee the computational accuracy. Because the structure is complex and irregular in the tube zone, the irregular tetrahedral mesh is applied in this zone to capture the heat transfer effectively. In addition, the hemisphere protrusions, the bleeding dimples and the LVGs are adopted with much finer unstructured tetrahedral mesh as shown in Fig. 4(b)–(d). Similar grid systems are employed for the cases of single tube.

Grid independence test is necessary to make sure the accuracy and validity of the numerical results. Here, we demonstrate the grid independence test of the tube rows with compound dimples and LVGs in detail. Four sets of grid numbers about 840,527, 1,186,595, 1,950,732 and 3,961,841 cells are examined and the obtained corresponding Nu numbers at $Re = 15,677$ are 67.20,

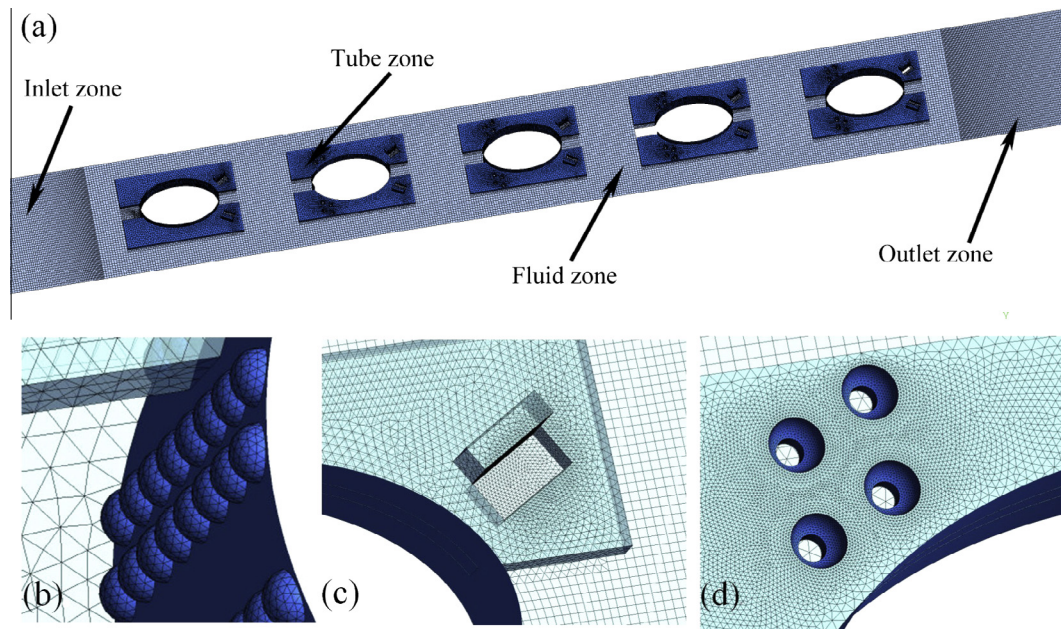


Fig. 4. Configuration of the computational domain mesh. (a) Computational domain mesh. (b) Hemisphere protrusion mesh. (c) LVG mesh. (d) Bleeding dimple mesh.

69.07, 70.11 and 71.24, respectively. The relative error of Nu between number 3 and number 4 is 1.58%, and the grid number of 1,950,732 is selected finally considering both the accuracy of the numerical results and the computer resource. Besides, similar tests of the grid independence are also performed for the single tube cases mentioned above. The detail results are not shown here to save the article's space.

2.5. Validation of the computational model

Apart from the grid-independency test, we should verify the computation accuracy of the model and calculation method. Because there is no available experimental data for the same physical model as in the present research, the H-type finned tube bank is carried out for the validation. The simulated geometry parameters of the H-type finned oval tube are the same with the ones presented in Ref. [42]. The experimental correlations from Ref. [42] for the Nusselt number and Euler number are presented as $Nu = 0.09152 Re^{0.7013} Pr^{0.33}$ and $Eu = 0.2963 Re^{-0.449}$, respectively. The inlet velocity is 5–9 m/s corresponding to Reynolds number from 22,504–40,509. The comparison of numerical results with

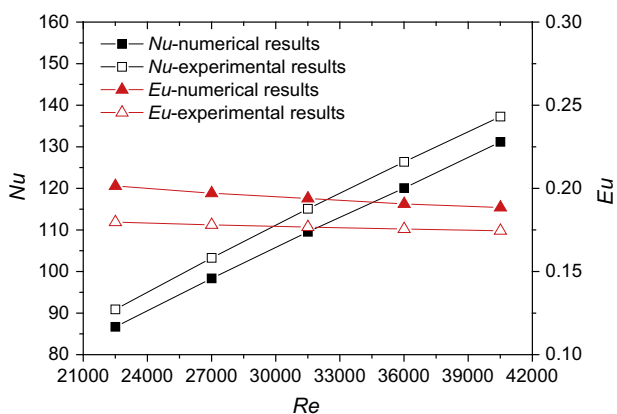


Fig. 5. Model validation with experimental data.

the corresponding experimental correlations is displayed in Fig. 5. The average discrepancy and maximum discrepancy between the predicted Nu and the experimental correlation are 5.0% and 5.2%, respectively, and the average discrepancy and maximum discrepancy between the predicted Eu and the experimental correlation are 8.9% and 10.8%, respectively. The good agreement between the predicted and experimental results indicates that the present computational model and numerical method are reliable to predict heat transfer and flow characteristics.

3. Numerical results and discussion

In the following sections, the longitudinal vortices generated by the rectangular winglet and dimples are presented first. Then heat transfer and anti-wear characteristics based on the single H-type finned oval tube with different enhanced structures are analyzed. Finally, the comparisons of the heat transfer and erosion characteristics between the original in-line H-type finned oval tube bank and the novel H-type finned oval tube bank designed with compound dimple-LVG and hemisphere protrusions on the first row of tube are presented.

3.1. Influence of rectangular winglet and dimples on flow field

Fig. 6 presents the streamlines starting near dimples for $u = 7$ m/s at $x = -26$ mm. When the gas flows over the dimples, the gas develops cyclones inside the dimples as shown in Fig. 6(b). Zhang et al. [43] pointed that the pits in the surface could decrease both the turbulence intensity near the wall surface and the friction resistance through lowering the velocity gradient. That is because the low speed cyclones inside the pits lead to interaction between the inner flow and the outer flow of the dimples called air cushion, which is the fluid control behavior on the wall boundary layer developed by dimples surface. The friction drag generated from the bottom of dimples also acts as an accessional impetus. Most of the gas stream inside the dimples flows downstream along the streamwise direction, and a small amount of residual gas flows to the back fin surface through the bleeding hole due to the pressure difference between the front fin surface and the back fin

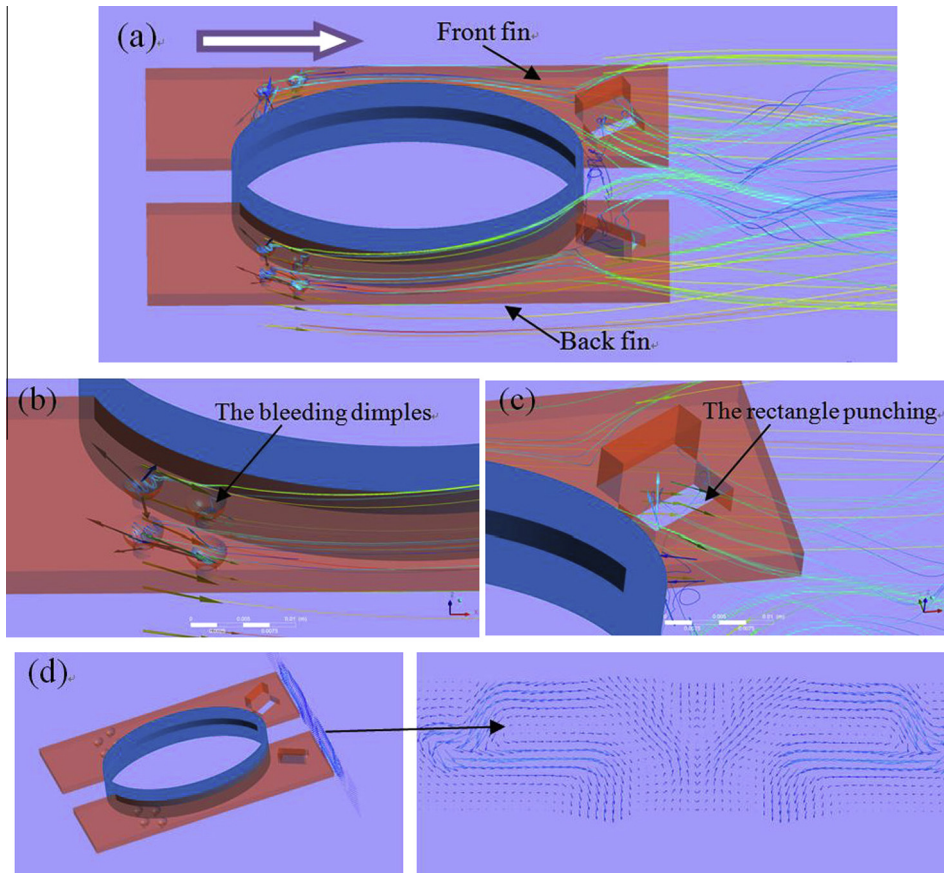


Fig. 6. Streamlines starting from the single tube near dimples in (a), (b) and (c), and velocity vectors of the cross-section at $x = 50$ mm behind the fin in (d).

surface, as displayed in Fig. 6(b). Furthermore, when flowing over the LVG, the air in the back surface flows to the front fin surface because the pressure on the front surface is lower than that on the back surface. The streamlines traversing across the fin through the bleeding hole and the LVG enhance strongly the fluid transport between the mainstream region and the wake region, which can be

observed from Fig. 6(a)–(c). Fig. 6(d) shows the velocity vectors of the cross-section at $x = 50$ mm behind the fin surface. It can be observed that the vortex is formed behind the fin, which is usually defined as the secondary flow. The structures of secondary flow generated by the LVG have been sufficiently studied and more details can be found in Ref. [44].

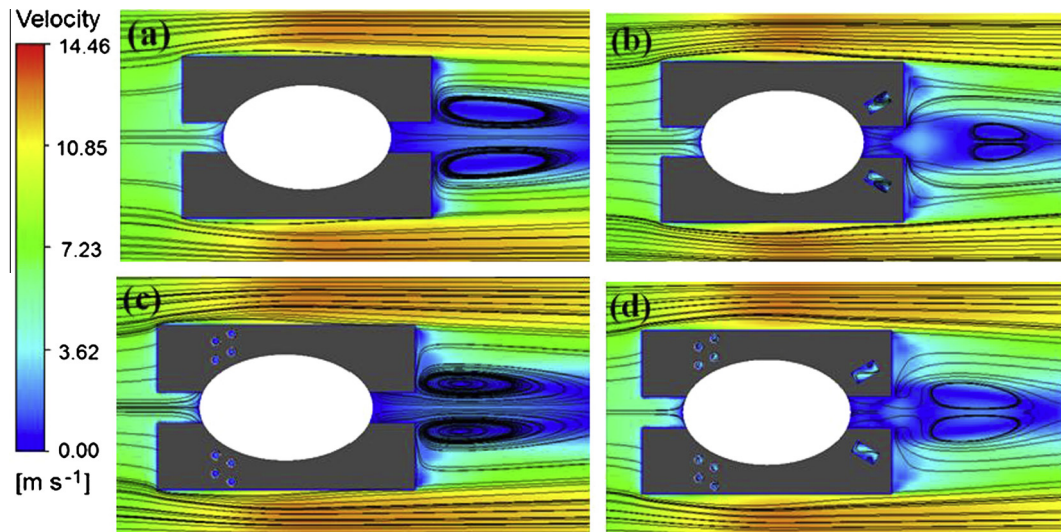


Fig. 7. Local velocity distribution on the middle cross-section in x direction. (a) H-type. (b) LVG. (c) Dimple. (d) Compound dimple-LVG.

3.2. Flow and heat transfer characteristics of single tube

Fig. 7 illustrates the local velocity distribution of the XY-plane in the middle-plane ($z = 0$) at $u = 7$ m/s. It can be seen that behind the tube, because of the obstruction of the tube, the gas separates into two regions, the mainstream region and the wake region. As can be observed from Fig. 7(a), the flow velocity is very low in the rear of the tube (the wake region). Behind the tube, we can clearly see from the streamlines distribution that the vortices are generated, which are called transverse vortices. The existence of the transverse vortices shows recirculating of the fluid in the wake region, where the fluid is almost separated from the main flow. The effect of dimples on the velocity field can be observed from Fig. 7(c). Compared with Fig. 7(a), the wake region in Fig. 7(c) is compressed and the streamlines in the centers of the transverse vortices become dense. Besides, comparing with Fig. 7(b) and (d) with Fig. 7(a), we can see that the wake region is reduced when the gas flows over the LVG. The LVG is able to strengthen the flow transport between the mainstream region and wake region so that enhance the flow of wake region and delay the flow separation behind the tube.

Fig. 8 presents the Nusselt number Nu and the pressure drop ΔP versus Reynolds number in which both the Nusselt number and pressure drop for all the cases increases with the increasing Reynolds number. The Nusselt numbers of the finned oval tubes with different heat transfer enhancement structures are significantly higher than the original H-type finned oval tube. For the three types of enhanced structures, the dimple, the LVG and the compound dimple-LVG, the enhanced heat transfer of the compound case achieves the highest, followed by the LVG case and the dimple case. Compared to the baseline, the increase of Nu for the three types of enhancement structures from low to high is 25.7–34.8%, 36.4–46.3%, and 44.7–49.9%, respectively. Similar results can be found for the pressure drop. The pressure drop from low to high is the baseline of H-type finned oval tube, the dimple, the LVG, and the compound dimple-LVG, respectively.

Fig. 9 shows the relationship between the friction factor and Reynolds number. It can be seen that the friction factor of the H-type finned oval tube with different augment structures are obviously higher than the original H-type finned oval tube. In addition, the friction factor from low to high is the dimple, the LVG, and the compound dimple-LVG cases, and the corresponding friction increase compared with the H-type finned oval tube is 34.7–37.5%, 48.5–51.8%, and 48.2–60.2%, respectively. However, at low Reynolds number, the friction factors for the tube with LVG and the tube with dimple-LVG are very close. The results suggest that the dimple could slow the speed of the friction increase at low

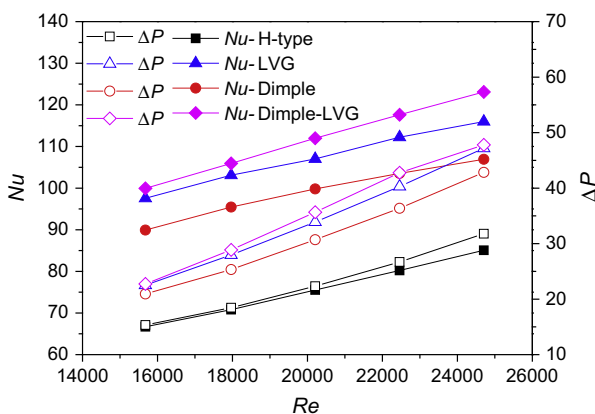


Fig. 8. Nusselt number and pressure drop versus Reynolds number.

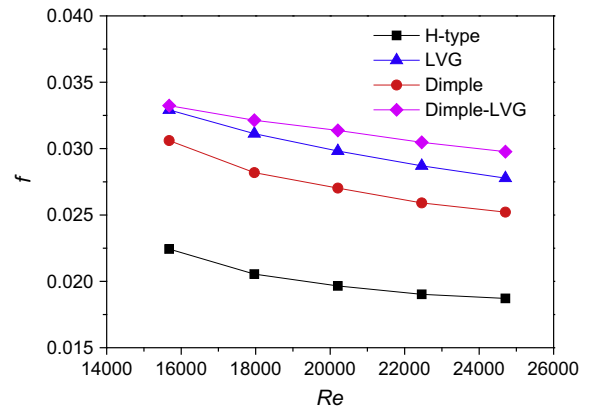


Fig. 9. Friction factor versus Reynolds number.

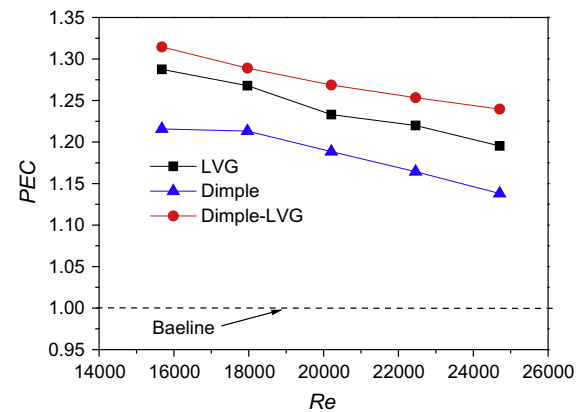


Fig. 10. PEC versus Reynolds number.

Reynolds number, and it is in consistent with the conclusion in Ref. [43].

Fig. 10 presents the parameter of PEC for the finned oval tube with different enhanced structures against Reynolds number. The PEC is a universal evaluation parameter which represents comprehensive performance of a heat transfer unit. The H-type finned oval tube is regarded as the compared baseline. From Fig. 10 we can see that the value of PEC from high to low is the compound dimple-LVG, the LVG, and the dimple. The compound dimple-LVG provides higher overall heat transfer performance than the LVG or the dimple, which is resulted from the hybrid effect. These results show that the tube with compound dimple-LVG case achieves considerable augmentation of heat transfer capacity with moderate flow resistance increase.

3.3. Erosion characteristics of single tube

Fig. 11 shows the erosion contours of the solid at $u = 7$ m/s. We can see that the fin erosion is mainly distributed on both verges of the fin, which can be explained that those zones have large flow speed and the erosion is proportional to the cube of particle speed. Because the augment structures, namely the dimples or LVGs, change the fluid field, the erosion loss of the solid tube and fin is decreased compared with the original H-type finned oval tube. Moreover, it can be seen that the maximum erosion of oval tube is concentrated in the range of 20–45° in windward of the oval tube.

From Fig. 12, we know that the tube wall erosion loss for H-type finned oval tube without any enhancement technique is the largest

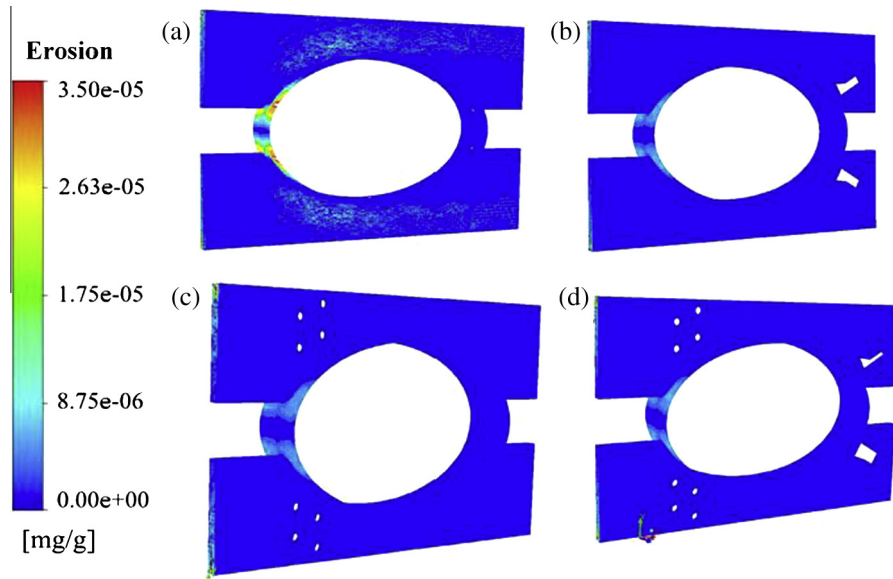


Fig. 11. Erosion contours of solid wall and fin. (a) H-type. (b) LVG. (c) Dimple. (d) Compound dimple-LVG.

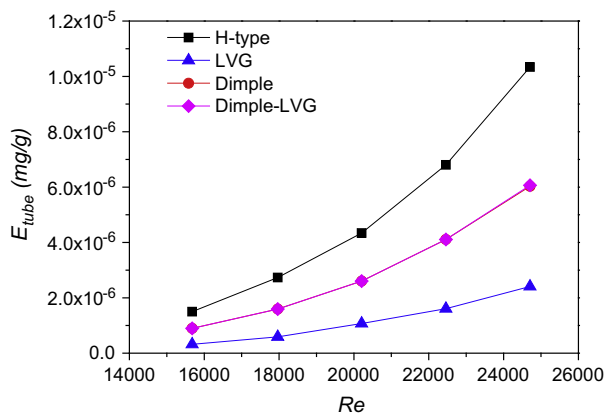


Fig. 12. Tube erosion value versus Reynolds number.

under the same Reynolds number. Specifically, compared with the H-type finned oval tube without any enhancement technique, the tube wall erosion loss of the compound dimple-LVG case and the dimple case is almost the same and reduced by 46.1–49.1%. The tube wall erosion loss for the H-type finned tube with rectangular LVG is reduced by 76.4–76.9%. Furthermore, the anti-wear performance of the enhanced tubes improves as the inlet velocity increases.

From the above results we can conclude that among the H-type finned tube with three types of enhanced heat transfer structures, the H-type finned oval tube with compound dimple-LVG performs the highest in heat transfer performance with moderate friction factor increase. At the same time, the anti-erosion performance of the H-type finned tube with the LVG works most efficiently. In the following sections, the compound dimple-LVG and LVG structures are chosen as the optimal heat transfer unit of the in-line five-row H-type finned oval tube bank. The in-line H-type finned oval tube bank is chosen as the baseline.

3.4. Optimized H-type finned oval tube bank with dimples and -30° LVGs of in-line arrangement

We firstly pay attention to the erosion characteristics of the first row of original H-type finned oval tube. In Fig. 13, the particle

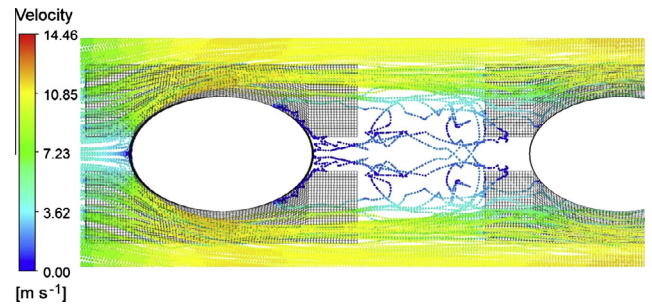


Fig. 13. Particle distribution on the first and second oval tubes of original H-type fin.

distribution on the first and second tubes is presented (For simplicity, the particle distribution on the rest tubes is not presented). It can be seen that most particles approach to the first tube directly. At the same time, because of the obstruction of the first tube, the amount of particles collided with the second tube is decreased. In addition, the velocity of collision with the second tube is reduced, so the wear of the first row tube would surpass the rest rows far. We have demonstrated that the H-type finned tube with LVG is of the highest anti-wear performance. So to reduce the wear loss of the first tube efficiently, the LVG is applied on the first tube, and further, inspired by the anti-wear bionics, we design the hemisphere protrusions on the windward of first tube as shown in Fig. 2(b). Note that though the LVG structure can reduce the erosion loss effectively, our preliminary investigation showed that the erosion loss of the first tube would be far more than the rest rows if only with the LVGs. So it is necessary to design hemisphere protrusions simultaneously.

Fig. 14 shows the three-dimensional streamline distribution among the tube rows at $u = 7$ m/s. We only show the streamline distribution among the first row, second row and third row tube for simplicity. As seen from Fig. 14(a), the transverse vortices are generated clearly behind the tubes. From Fig. 14(b), the streamline presents chaos and disorder. The LVGs behind the tubes traverse violently the fluid flow between the main region and weak region. We can also see that the cyclones are generated inside the dimples.

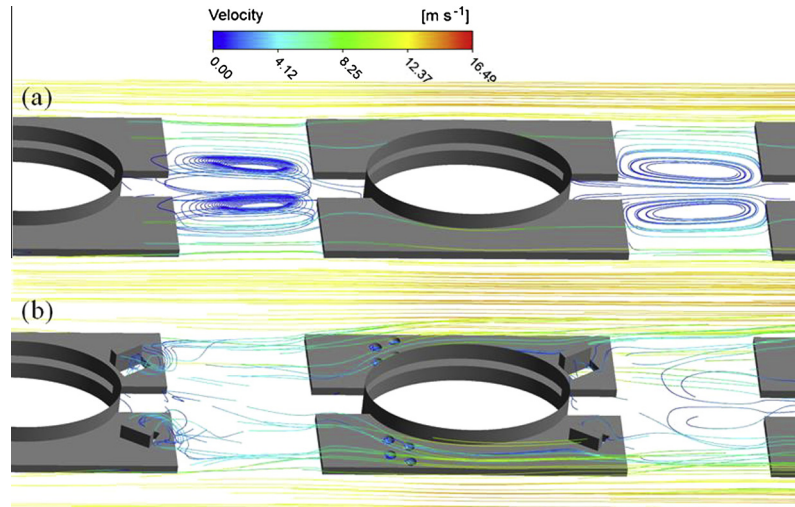


Fig. 14. Three-dimensional streamlines among tube rows.

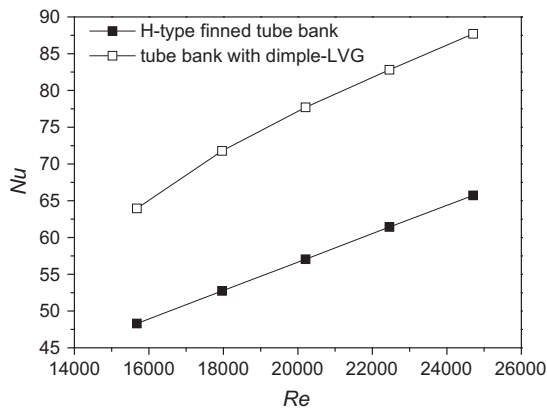


Fig. 15. Nusselt number versus Reynolds number for tube bank.

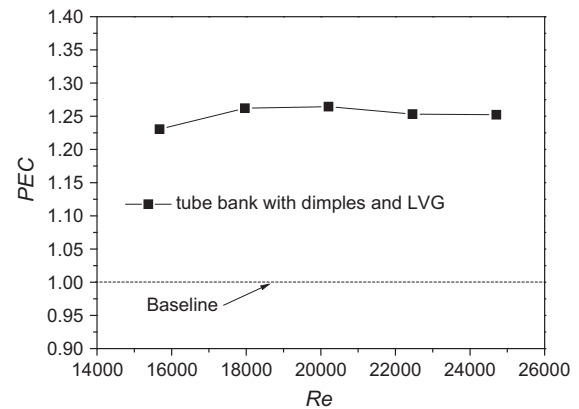


Fig. 17. PEC versus Reynolds number for tube bank.

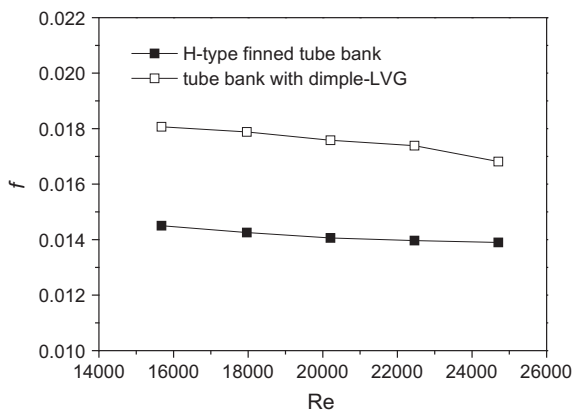


Fig. 16. Friction factor versus Reynolds number for tube bank.

As a whole, the effect of compound dimple-LVG on the velocity field delays the flow separation behind the tubes and disturbs the flow boundary strongly so that the heat transfer is improved greatly.

The Nusselt number versus Reynolds number is presented in Fig. 15. The Nusselt number of the tube bank with dimple-LVG is markedly higher than that of the original H-type finned tube bank

by 32.4–36.2%. Fig. 16 presents the friction factor versus the Reynolds number. Compared with the H-type finned tube bank, the friction factor of the tube bank with dimple-LVG is increased by 20–25.4%. The PEC versus the Reynolds number is presented in Fig. 17 in which the PEC of the original H-type finned tube bank is regarded as 1 (the baseline). The value of PEC of the tube bank with dimple-LVG is improved by 23–26.4%.

Fig. 18 illustrates the erosion contours on solid tube and fin at $u = 7$ m/s. For simplicity, we only present the first tube and second tube. Distribution of the wear of the remaining tube is similar to the second tube. Here we pay attention to the windward of the first tube. We know from the previous discussion that the maximum wear concentrates on the windward of tubes, and the anti-wear performance of H-type finned tube with LVG achieves the highest. In addition, the erosion loss of the first tube is much greater than that of the remaining tubes. So the first tube is designed with the hemisphere protrusions between about -40° and 40° in the windward side and the fin is adopted with the LVG structure. From Fig. 18(a) and (b), we can see that the wear loss of the first tube decreases obviously for the novel H-type finned oval tube bank.

The erosion loss against the Reynolds number is shown in Fig. 19. We can see that with the Reynolds number increasing, the erosion of both cases (the original H-type finned tube bank and the H-type finned tube bank with dimple-LVG) increases. It can be clearly observed that the erosion loss of the H-type tube bank with compound dimple-LVG is lower than that of the

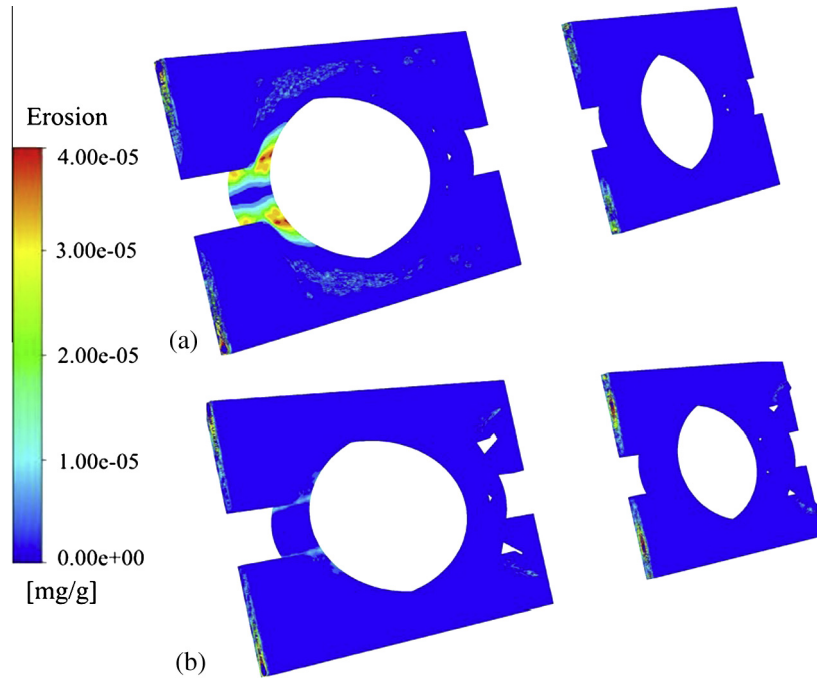


Fig. 18. Erosion contours on the solid walls and fins of tube bank. (a) Original H-type finned oval tube bank. (b) Novel H-type finned oval tube bank with dimple-LVG.

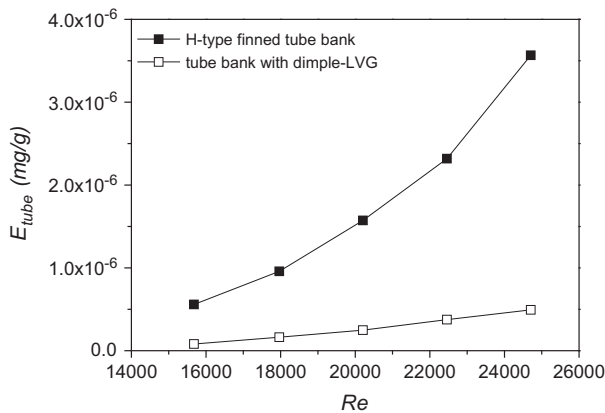


Fig. 19. Tube erosion value versus Reynolds number for tube bank.

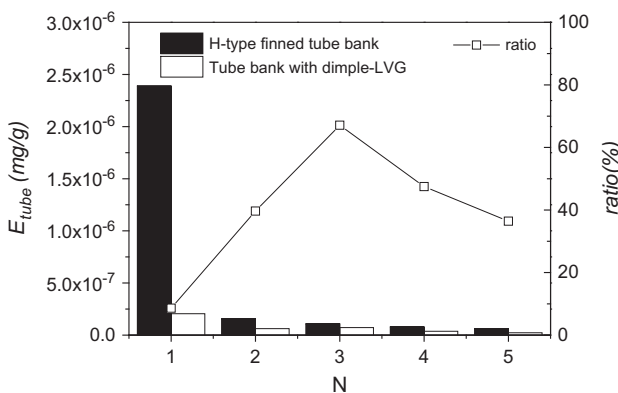


Fig. 20. Erosion loss of each tube and erosion ratio of the new H-type finned tube bank with dimple-LVG to original H-type finned tube bank.

baseline, and the larger of Reynolds number, the higher improvement of the anti-wear performance.

Fig. 20 presents the erosion loss of each tube and the erosion loss ratio of the H-type finned tube bank with dimple-LVG to the original H-type finned tube bank at $u = 7$ m/s. The horizontal axis represents the row number. The erosion ratio increases firstly and then decreases. Specially, for the first row of novel tube bank, the wear loss is greatly decreased. In addition, the erosion ratio of the first tube is far less than unity, which indicates that the hemisphere protrusions work well in anti-wear performance. Additionally, there is no obvious difference between the enhanced structure and the baseline for the tube erosion from the second row to fifth row. This can be explained as follows: (1) for the H-type finned oval tube bank, the obstruction of the first row of tube plays the main role so the wear loss of the rest tubes is reduced greatly and the wear loss reduction mainly concentrates on the windward side; (2) for the H-type finned tube bank with dimple-LVG, affected by the heat transfer augment structures, when the particles impact to the tube in the rear, they would rebound and collide with the front-row tube. The increase in wear loss focuses on the leeward side. As a whole, most of the erosion loss is resulted from the collision between the particles and the tube windward side. The present H-type finned oval tube with compound dimple-LVG structure and together with the bio-inspired protrusion design on the first tube can be considered as a candidate for improving the performance of both heat transfer and anti-wear.

4. Conclusions

In this study, the heat transfer and erosion characteristics of the H-type finned oval tube, tube with LVGs, tube with bleeding dimples, and tube with compound dimples and LVGs have been numerically studied. The following conclusions are obtained.

1. The comprehensive performance of the enhanced heat transfer surfaces is evaluated by the parameter PEC. The H-type finned oval tube with compound dimples and LVGs provides the highest overall heat transfer performance. The performance of the

tube with LVG is lower than that of the tube with compound dimple-LVG, and the tube with bleeding dimple presents the lowest performance.

- The anti-wear performance of the tube with LVGs is the highest, and it is obviously higher than that of the tube with compound dimple-LVG and with the sole dimples. For all the enhanced structures, the erosion loss of the tubes are dramatically less than the original H-type oval tube, and the reduction of erosion loss gets more for a larger Reynolds number.
- When designing the tube bank, we take advantage of the superiority of the LVG and the compound dimple-LVG. The first row is designed with the LVG for anti-erosion while the rest rows with the compound dimple-LVG for heat transfer enhancement in accordance with the nonuniformity rule. We also apply the hemisphere protrusions in the windward of the first row of tube, inspired by the bionics. Such an optimized H-type finned oval tube bank heat exchanger can improve both the heat transfer and anti-wear performance greatly.

The optimized H-type finned oval tube bank heat exchanger in present paper may have significant applications not only to improve the heat transfer efficiency and economy, but also reduce the wear loss of heat exchanger and promote the safe operation level in coal-fired boilers.

Acknowledgments

This work is supported by the National Basic Research Program of China (973 Program) (No. 2011CB710702) and the National Natural Science Foundation of China (No. 51222604).

References

- Marner WJ, Bergles AE, Chenoweth JM. On the presentation of performance data for enhanced tubes used in shell-and-tube heat exchangers. *ASME J Heat Transfer* 1983;105:358–65.
- Chen HX, Xu JL, Li ZJ, Xing F, Xie J. Stratified two-phase flow pattern modulation in a horizontal tube by the mesh pore cylinder surface. *Appl Energy* 2013;112:1283–90.
- Chen HX, Xu JL, Li ZJ, Xing F, Xie J, Wang W, et al. Flow pattern modulation in a horizontal tube by the passive phase separation concept. *Int J Multiphas Flow* 2012;45:12–23.
- Zhang YH, Wu X, Wang LB, Song KW, Dong YX, Liu S. Comparison of heat transfer performance of tube bank fin with mounted vortex generators to tube bank fin with punched vortex generators. *Exp Therm Fluid Sci* 2008;33:58–66.
- Joardar A, Jacobi AM. Heat transfer enhancement by winglet-type vortex generator arrays in compact plain-fin-and-tube heat exchangers. *Int J Refrig* 2008;31:87–97.
- Promvong P, Thianpong C. Thermal performance assessment of turbulent channel flows over different shaped ribs. *Int Commun Heat Mass Transfer* 2008;35:1327–37.
- Tian LT, He YL, Tao YB, Tao WQ. A comparative study on the air-side performance of wavy fin-and-tube heat exchanger with punched delta winglets in staggered and in-line arrangements. *Int J Thermal Sci* 2009;48:1765–76.
- Li J, Wang SF, Chen JF, Lei YG. Numerical study on a slit fin-and-tube heat exchanger with longitudinal vortex generators. *Int J Heat Mass Transfer* 2011;54:1743–51.
- He YL, Han H, Tao WQ, Zhang YW. Numerical study of heat-transfer enhancement by punched winglet-type vortex generator arrays in fin-and-tube heat exchangers. *Int J Heat Mass Transfer* 2012;55:5449–58.
- Bilir L, Ozerdem B, Ereke A, Ilken Z. Heat transfer and pressure drop characteristics of fin-tube heat exchangers with different types of vortex generator configurations. *J Enhanc Heat Transfer* 2010;17:243–56.
- Wu JM, Zhang H, Yan CH, Wang Y. Experimental study on the performance of a novel fin-tube air heat exchanger with punched longitudinal vortex generator. *Energy Convers Manage* 2012;57:42–8.
- Yakut K, Sahin B, Celik C, Alemdaroglu N, Kurnuc A. Effects of tapes with double-sided delta-winglets on heat and vortex characteristics. *Appl Energy* 2005;80:77–95.
- Pesteei SM, Subbarao PMV, Agarwal RS. Experimental study of the effect of winglet location on heat transfer enhancement and pressure drop in fin-tube heat exchangers. *Appl Therm Eng* 2005;25:1684–96.
- Chen Y, Fiebig M, Mitra NK. Heat transfer enhancement of a finned oval tube with punched longitudinal vortex generators in-line. *Int J Heat Mass Transfer* 1998;41:4151–66.
- Chen Y, Fiebig M, Mitra NK. Conjugate heat transfer of a finned oval tube with a punched longitudinal vortex generator in form of a delta winglet-parametric investigations of the winglet. *Int J Heat Mass Transfer* 1998;41:3961–78.
- Chen Y, Fiebig M, Mitra NK. Heat transfer enhancement of finned oval tubes with staggered punched longitudinal vortex generators. *Int J Heat Mass Transfer* 2000;43:417–35.
- Yang KS, Wun KL, Chen IY, Wang CC. Experimental investigation of high performance thermal module with dimple vortex generators. *Int Microsys Pack Assem Circuits Technol* 2010;1–4 [5th IMPACT].
- Vicente PG, Garcia A, Viedma A. Heat transfer and pressure drop for low Reynolds turbulent flow in helically dimpled tubes. *Int J Heat Mass Transfer* 2002;45:543–53.
- Bi C, Tang GH, Tao WQ. Heat transfer enhancement in mini-channel heat sinks with dimples and cylindrical grooves. *Appl Therm Eng* 2013;55:121–32.
- Lee J, Lee KS. Correlations and shape optimization in a channel with aligned dimples and protrusions. *Int J Heat Mass Transfer* 2013;64:444–51.
- Grant G, Tabakoff W. Erosion prediction in turbomachinery resulting from environmental solid particles. *J Aircr* 1975;12:471–8.
- Hutchings IM, Winter RE. Particle erosion of ductile metals: a mechanism of material removal. *Wear* 1974;27:121–8.
- Winter RE, Hutchings IM. Solid particle erosion studies using single angular particles. *Wear* 1974;29:181–94.
- Nagarajan R, Ambedkar B, Gowrisankar S, Somasundaram S. Development of predictive model for fly-ash erosion phenomena in coal-burning boilers. *Wear* 2009;267:122–8.
- Lee BE, Fletcher CAJ, Behnia M. Computational study of solid particle erosion for a single tube in cross flow. *Wear* 2000;240:95–9.
- Rahimi M, Khoshhal A, Shariati M. CFD modeling of a boiler's tubes rupture. *Appl Therm Eng* 2006;26:2192–200.
- Schade KP, Erdmann H, Hadricha T, Schneider H, Frank T, Bernert K. Experimental and numerical investigation of particle erosion caused by pulverised fuel in channels and pipework of coal-fired power plant. *Power Technol* 2002;125:242–50.
- Wang YF, Yang ZG. Finite element model of erosive wear on ductile and brittle materials. *Wear* 2008;265:871–8.
- Sundararajan G, Roy M. Solid particle erosion behaviour of metallic materials at room and elevated temperature. *Tribol Int* 1997;30:339–59.
- Fan JR, Zhou DD, Jin J, Cen KF. Numerical simulation of tube erosion by particle impaction. *Wear* 1991;142:171–84.
- Fan JR, Zhou DD, Zeng KL, Cen KF. Numerical and experimental study of finned tube erosion protection methods. *Wear* 1992;152:1–19.
- Fan JR, Sun P, Zheng YQ, Zhang XY, Cen KF. A numerical study of a protection technique against tube erosion. *Wear* 1999;225:458–64.
- Fan JR, Sun P, Chen LH, Cen KF. Numerical investigation of a new protection method of the tube erosion by particles impingement. *Wear* 1998;223:50–7.
- Dodds D, Naser J, Staples J, Black C, Marshall L, Nightingale V. Experimental and numerical study of the pulverised-fuel distribution in the mill-duct system of the Loy Yang B lignite fuelled power station. *Powder Technol* 2011;207:257–69.
- Dodds D, Naser J. Numerical study of the erosion within the pulverised-fuel mill-duct system of the Loy Yang B lignite fuelled power station. *Powder Technol* 2012;217:207–15.
- Speziale CG, Thangam S. Analysis of an RNG based turbulence model for separated flows. *Int J Eng Sci* 1992;30:1379–88.
- Saffman PG. The lift on a small sphere in a slow shear flow. *J Fluid Mech* 1965;22:385–400.
- Tabakoff W, Kotwal R, Hamed A. Erosion study of different materials affected by coal ash particles. *Wear* 1979;52:161–73.
- Sommerfeld M. Theoretical and experimental modeling of particulate flows. *Lect Ser: Von Karman Inst.*; 2000.
- Solnordal CB, Wong CY, Zambari A, Jadid M, Johar Z. Determination of erosion rate characteristic for particles with size distributions in the low Stokes number range. *Wear* 2013;305:205–15.
- Holman JP. *Heat Transfer*. 10th ed. China Machine Press; 2011.
- Liu YZ, Yuan YC, Xu SY, Wu WB. Experimental study on the characteristics of heat transfer and flow resistance for H-type finned tube banks. *J Univ Shanghai Sci Technol* 2004;26:457–60 [in Chinese].
- Zhang CC, Ren LQ, Wang J, Zhang YZ. Simulation on flow control for drag reduction of revolution body using bionic dimpled surface. *Acta Armamentarii* 2009;30:1066–72 [in Chinese].
- Chang LM, Wang LB, Song KW, Sun DL, Fan JF. Numerical study of the relationship between heat transfer enhancement and absolute vorticity flux along main flow direction in a channel formed by a flat tube bank fin with vortex generators. *Int J Heat Mass Transfer* 2009;52:1794–801.